



HAL
open science

FAST-Hex -A Morphing Hexarotor: Design, Mechanical Implementation, Control and Experimental Validation

Markus Ryll, Davide Bicego, Mattia Giurato, Marco Lovera, Antonio Franchi

► To cite this version:

Markus Ryll, Davide Bicego, Mattia Giurato, Marco Lovera, Antonio Franchi. FAST-Hex -A Morphing Hexarotor: Design, Mechanical Implementation, Control and Experimental Validation. IEEE/ASME Transactions on Mechatronics, 2022, 27 (3), pp.1244 - 1255. 10.1109/TMECH.2021.3099197. hal-03271812

HAL Id: hal-03271812

<https://laas.hal.science/hal-03271812>

Submitted on 27 Jun 2021

HAL is a multi-disciplinary open access archive for the deposit and dissemination of scientific research documents, whether they are published or not. The documents may come from teaching and research institutions in France or abroad, or from public or private research centers.

L'archive ouverte pluridisciplinaire **HAL**, est destinée au dépôt et à la diffusion de documents scientifiques de niveau recherche, publiés ou non, émanant des établissements d'enseignement et de recherche français ou étrangers, des laboratoires publics ou privés.

FAST-Hex – A Morphing Hexarotor: Design, Mechanical Implementation, Control and Experimental Validation

Markus Ryll^{1,4}, Davide Bicego^{1,2}, Mattia Giurato³, Marco Lovera³ and Antonio Franchi^{1,2}

Abstract—We present FAST-Hex, a micro aerial hexarotor platform that allows to seamlessly transit from an *under-actuated* to a *fully-actuated* configuration with only one additional control input, a motor that synchronously tilts all propellers. The FAST-Hex adapts its configuration between the more efficient but under-actuated, collinear multi-rotors, and the less efficient but full-pose-tracking, which is attained by non-collinear multi-rotors. On the basis of prior work on minimal input configurable micro aerial vehicle, we mainly stress three aspects: mechanical design, motion control, and experimental validation. Specifically, we present the lightweight mechanical structure of the FAST-Hex that allows to only use one additional input to achieve configurability and full actuation in a vast state space. The motion controller receives as input any reference pose in $\mathbb{R}^3 \times \text{SO}(3)$ (3D position + 3D orientation). Full pose tracking is achieved if the reference pose is feasible with respect to actuator constraints. In case of unfeasibility, a new feasible desired trajectory is generated online giving priority to the position tracking over the orientation tracking. Finally, we present a large set of experimental results shading light on all aspects of the control of the FAST-Hex.

I. INTRODUCTION

Unmanned aerial vehicles (UAVs) are used in a wide spectrum of applications like environmental and infrastructural monitoring and aerial photography, search and rescue operations and aerial physical interaction, including transportation, sensing by contact, and assembly tasks, just to name a few. These very different applications resulted in a broad potpourri of differently shaped UAVs. For high-altitude, long-duration surveillance applications a fixed-wing UAV is the optimal candidate. For applications in confined and cluttered environments a small quadrotor UAV might be better suited. For aerial manipulation a fully-actuated multirotor UAV might be the optimal candidate. Each of these UAV configurations has benefits and drawbacks in certain applications.

A. Literature Overview

As applications for UAVs become more complex, with different requirements along their missions, morphable UAVs appeared. Systems of the class of morphable UAVs can change their configuration, optimizing the UAV's shape depending on a local task along the mission.

In [1] and [2] aerial robots are presented that are able to translate the position of their propellers to squeeze through

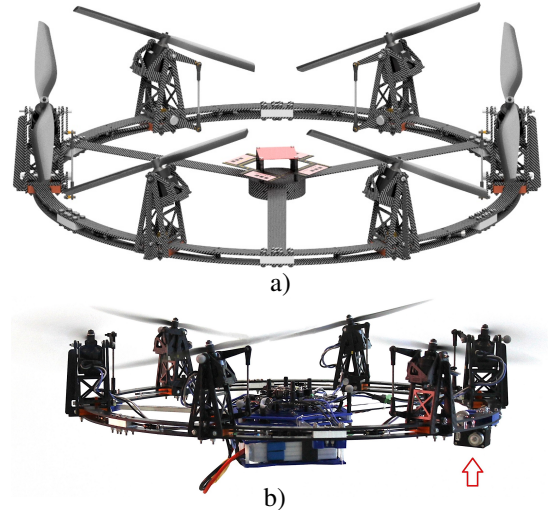


Fig. 1. a) CAD prototype of the FAST-Hex. All propellers are tilted in a synchronized manner by a single motor. b) Flying prototype with tilted propellers. The single servomotor for tilting all propellers is visible on the right bottom side of the ring structure and highlighted with an arrow.

narrow gaps. For space-efficient storing and high speed ejection the quadrotor UAV in [3] has a body-drag optimized shape in folded configuration that unfolds for normal flight. In [4]–[6] a snake-like multirotor platform is described, that can translate through air and grasp objects.

A particular subset of morphable aerial robots achieve control of their body pose beyond the classical position and yaw orientation tracking. The authors of [7] present an aerial robot that can tilt a part of its frame in order to gain independent control of the vehicle's pitch angle, while the authors of [8] lock the UAV's inner body in a gimbal system to achieve full pose tracking with the inner body. To allow full independent tracking of position and orientation trajectories the multirotor UAVs in [9]–[12] can actively tilt all their propellers. This class of fully-actuated non-collinear multi-rotor systems has emerged as a class of UAVs benefiting from fast disturbance rejection [13]–[16] and full-pose trajectory tracking (independent tracking of a desired 3D position and 3D orientation [17]–[23]). Furthermore, fully-actuated aerial vehicles are able to track a wrench profile (independent force and torque trajectories) making them optimal candidates as aerial-physical interaction tools.

Technical solutions for fully-actuated aerial vehicles are currently implemented following two paradigms. Aerial vehicles of the first paradigm have their propellers fixed in a particular tilting angle (see our previous works [20], [24]) and do not belong to the group of morphable drones. These systems have simpler mechanics, lower control complexity and are usually lighter as no additional actuators are required, but suffer from increased energy consumption due to unavoidable, parasitic internal forces and a usually smaller volume of admissible

¹LAAS-CNRS, Université de Toulouse, CNRS, Toulouse, France

²Robotics and Mechatronics Lab, Faculty of Electrical Engineering, Mathematics & Computer Science, University of Twente, Enschede, The Netherlands, d.bicego@utwente.nl, a.franchi@utwente.nl

³Dipartimento di Scienze e Tecnologie Aerospaziali, Politecnico di Milano, Italy, mattia.giurato@polimi.it, marco.lovera@polimi.it

⁴Technical University of Munich, Germany, Department of Aerospace and Geodesy, Professorship of Autonomous Aerial Systems, markus.ryll@tum.de

This work has been partially funded by the European Union's Horizon 2020 research and innovation program under grant agreement ID: 871479 AERIAL-CORE.

wrench. Systems of the second paradigm can change the pose of the propellers, allowing thrust vectoring of every single propeller (cf. [11], [12], [19]). While these systems commonly enable tracking of a larger or tunable volume of admissible wrench and therefore waste less energy, the mechanics and the control of these systems are more complex, and the weight is increased by the number of required actuators, decreasing the overall flight time.

B. Contribution of this work

In this article, we present the Fully-Actuated by Synchronized-Tilting Hexarotor (*FAST-Hex*), with six propellers actively tiltable by only one additional motor (see Fig. 1 a) & b). The design goal of the *FAST-Hex* was to develop an aerial vehicle with the capability of tracking a wrench profile in a large volume while maximizing the flight time. Most common mission scenarios for fully-actuated aerial vehicles do not require full actuation during the full flight-time but only during a period of the mission (e.g., while conducting manipulation tasks or complex obstacle avoidance maneuvers). For the rest of the mission underactuated flight is sufficient. Aerial platforms of the first paradigm (Sec. I-A) are always fully actuated resulting in a reduced flight time due to the parasitic internal forces. Platforms of the second paradigm require a number of additional actuators to enable the thrust vectoring, resulting in a higher mass and an as well reduced flight time. For the *FAST-Hex* we decided to use only one actuator. This additional control input drives the configuration of the aerial platform in a continuum of configurations between the energetically very efficient but under-actuated configuration and the less efficient but maximally actuated configuration. The mechanical parts, distributing the actuation are designed, having lightness in mind. By designing a combination between under- and fully-actuated platforms by means of only one additional servomotor, we enable high-level fine tuning between maximal efficiency and decoupled wrench tracking for the task at hand.

This paper is an extension of work originally presented in [25] and [26] where the theoretical idea of the *FAST-Hex* and an extension of the control concepts have been presented.

The contribution of the paper is first, the presentation and discussion of the mechanics of the *FAST-Hex* prototype, that uses only one additional motor for actuating coordinately all propellers. To increase rigidity the prototype overcomes the common star-form of multirotors by presenting a lightweight ring-structure. Second, we present an improved version of the pose-tracking controller presented in [26], making it more suitable for such morphable platform. The pose tracking controller uses as input an arbitrary, desired full pose trajectory in $\mathbb{R}^3 \times \text{SO}(3)$ while the controller updates the orientation tracking, when strictly needed to overcome spinning rate saturations of any propeller. While this controller finds its perfect application in systems that can seamlessly transition between under and fully-actuated systems, it is applicable to any multi-rotor platform. The third contribution is a broad set of experiments conducted with the *FAST-Hex* prototype.

The paper is structured as follows. We first present the mechanical system of the *FAST-Hex* and then derive the

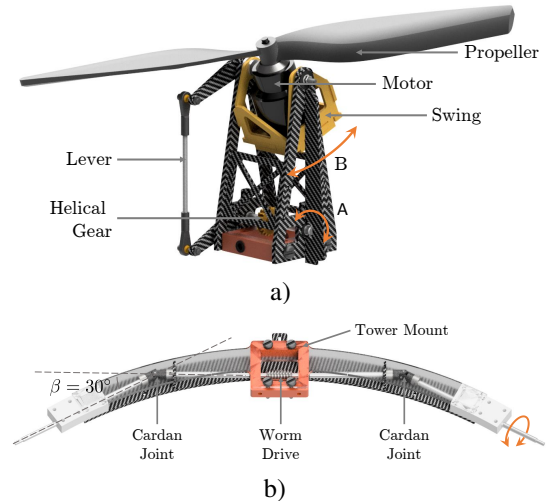


Fig. 2. a) CAD model of a single motor tower. A worm drive actuates the helical gear indicated by ‘A’ in the figure. The helical gear is rigidly connected on an axle, that is linked to a lever. The lever actuates a swing, which hosts the motor. The swing construction is used to rotate the the propeller close to its center. b) The complete MAV consists of six of the depicted elements. The top part of the ring is drawn transparent, allowing to see inside the ring structure. A single motor (not depicted in this figure) actuates the axes in the ring structure, that are connected with cardan joints. The direction of the worm drives is alternating, allowing the opposing rotation of neighboring motors.

dynamical model in Sec. II and III. In Sec. IV we describe the full-pose geometric control in $\mathbb{R}^3 \times \text{SO}(3)$ for generic multi-rotor platforms. In Sec. V we present a broad spectrum of experimental results. Finally, Sec. VI concludes the paper with a summary of the results and an outline of future work.

II. MECHANICAL DESIGN

In this section we will describe the mechanical and electrical design of the *FAST-Hex* prototype.

We designed a Micro Aerial Vehicle (MAV) that inherits the benefits of both under- and fully-actuated vehicles, namely the possibility for energy efficient flight, e.g., for cruising and the ability for independent position and orientation control, e.g., for aerial manipulation or advance maneuvering in cluttered environments, while minimizing additional inputs, electromechanical components and weight. Thanks to their simple mechanical design, the most common fully-actuated MAVs are hexarotor systems composed by alternatingly fixed tilted propellers [20], [24]. These systems allow for full actuation in a limited state space of the MAV, depending on the tilt angle of the propellers. The larger the tilting angle, the more the platform is able to generate lateral forces but at the cost of higher internal forces, reducing the efficiency and flight-time of these platforms. The *FAST-Hex* is inspired by this MAV type. We aimed to be able to change the tilting angle while flying with a minimum set of additional inputs, namely only one additional actuator (see Fig. 1-b). Therefore, the actuation of the single motor needs to be transmitted to all propellers (see Fig. 2 and the attached video). To achieve this objective, all motors are arranged on a regular ring structure of radius l (where $l = 0.305$ m in our prototype). The propellers are mounted on-top of six motor towers (see Fig. 2-a and Fig. 3), which are evenly spaced on the ring planar structure and therefore 60° apart. In order to simplify the motion model and minimizing

the translation of the thrust generation points (*i.e.*, the center of the propellers) we aimed to rotate the propellers as close as possible to the rotation center of the blades. Therefore, we designed the swing mechanism, rotating the propellers less than 1 cm away from their rotation centres (see Fig. 2-a). The motors with the propellers are mounted in the swings on the top of the tower. They are rigidly connected via a lever mechanism to a worm drive with a high gear ratio (20:1) placed at the base of the tower. The worm drive offers self blocking capabilities, minimal play, and precise control of the desired tilting angle and a marginal hysteresis effect. Inside the structural ring there are 11 carbon fibre axles, forming a polygon inscribed in the ring, all connected by Cardan joints (also known as universal joints): these allow the propagation of the rotation of the bars throughout the ring, see Fig. 2-b & 3. The central axle is attached to a motor actuating the system. Consequently, the propulsive groups 1-2-3 and 6-5-4 are actuated by two separate chains departing both from the same servo motor, a Dynamixel MX-28T, comprising a Maxon DC motor, a CORTEX-M3 micro-controller and a 12 bit contactless encoder. Splitting the whole chain in two sub-chains greatly reduces friction phenomena and torsion effects of the carbon fibre parts, which, in the case of longer chains, could induce jerky movements on the parts located far from the motor box due to intrinsically present friction phenomena. Every second axles is endowed with the aforementioned worm drive (a worm-shaft coupled with a worm gear), that is responsible for the transmission of the rotation to the corresponding motor tower. The worm shafts and the gears are realized with a high-precision 3D-printer. The maximum absolute value of the tilting angle (mechanically limited) is $\bar{\alpha} = 35^\circ$.

Cardan joints have the well known property of an unequal input angle γ_{j-1} and output angle γ_j during a full rotation, depending on the bending angle β . As depicted in Fig. 3, there is one universal joint between the servo motor and the worm drive actuating propeller 1 and propeller 6, three universal joints to propeller 2 and propeller 5, and finally five joints to propeller 3 and propeller 4. To understand the effect size of this parasitic effects on the actual propeller tilting angles α_i , we modeled the full drive train. Let us define γ_j as the rotation angle of an axle placed downstream of a chain of j previous universal joints. The actual propeller tilting angle α_i depends on the desired tilting angle α_{des} , the transmission ratio k of the worm drives, and the propeller number (see Fig. 3), can be found in a recursive way as

$$\begin{aligned} \gamma_0 &= \frac{1}{k} \alpha_{des}, \\ \gamma_j &= \text{atan2}(\sin \gamma_{j-1}, \cos \beta \cos \gamma_{j-1}) \quad j \in [1, 5], \\ \alpha_i &= k (-1)^{i-1} \gamma_{(6-|2i-7|)} \quad i \in [1, 6]. \end{aligned} \quad (1)$$

A comparison of the desired and the actual angles is depicted in Fig. 4. The worm drives, with a transmission ratio of $k = 0.05$, reduce the parasitic effect. The analytically maximum tracking difference for the two propellers with the most Cardan joints in between (propeller 3 and propeller 4) is approximately 1° . The actual tracking error (e.g., due to bending, mechanical imprecision, play) of the desired tilting angle is below 2° . We

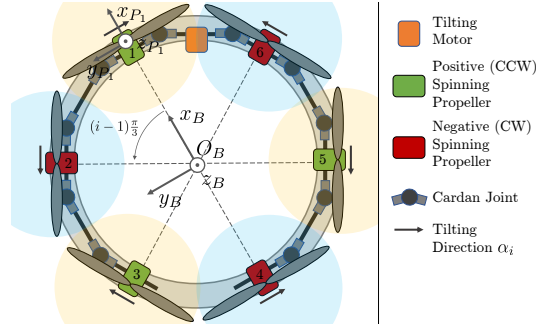


Fig. 3. A sketch of the simplified model of FAST-Hex highlighting major mechanical components and the tilting directions of the six swings inside the motor towers. Counter-clockwise spinning propellers $\{1, 3, 5\}$ are depicted in light-orange, while the clockwise spinning ones $\{2, 4, 6\}$ in light-blue.

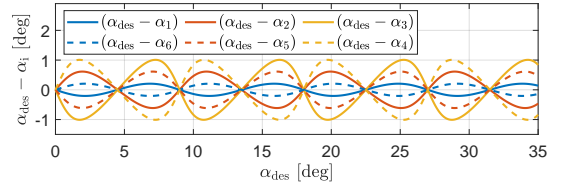


Fig. 4. Error between desired α_{des} and actual tilting angle α_i for the FAST-Hex for all six propellers. The absolute peak divergence is approximately 1° . Therefore it has been decided not to consider it in the control design but to treat it as disturbance.

will therefore neglect this relatively small difference and will let the controller (Sec. IV) cope with it. The overall structure of the ring gives a high rigidity to the system, reducing the vibrations of the motors, compared to the typical arm structure of multi-rotor systems. Mechanical details of the system are listed in Table I.

The electronics, including an inertial measurement unit (IMU) and six brushless motor controllers, are mounted in the center of the ring structure, decoupling parasitic vibrations from the motors. The IMU and the motor controllers are available off-the-shelf from Mikrokooper. The remaining hardware is composed by six MK3638 motors, controlled by six BL-Ctrl V2.0 brushless controllers, and driving six EPP1245 propellers (12 inch of diameter and 4.5 inch of pitch). The electronic speed controllers allow to precisely control the propeller spinning velocity using a closed loop sliding-mode controller [27]. The speed controllers are connected to a Flight-Ctrl V2.5 board, equipped with the IMU hosting three ADXRS620 gyroscopes and a Memsic MXR9500M 3D accelerometer.

The total mass of the FAST-Hex is 3.1 kg, including a ≈ 400 g battery. The total mass of all parts that are part of the tilting actuation (e.g., motor, gears, joints, axles) is ≈ 380 g. The mass could clearly be reduced by performing an optimizing over the first prototype (e.g., reduce the number of metal screws, reducing material thickness, etc.).

III. MODELING

A photograph and a CAD model of the actual FAST-Hex are shown in Fig. 1. We will now introduce a simplified mathematical model of the FAST-Hex that we will utilize deriving the controller in Sec. IV. A sketch of the simplified model is depicted in Fig. 3 showing the relevant reference

TABLE I
MECHANICAL, PHYSICAL AND CONTROL PARAMETERS

Part	Symbol	Value
Ring ext. diameter	d	640 mm
Propeller diameter		12 inch (≈ 30.5 cm)
Propeller tilting angle	α_i	$(-1)^{i-1} \alpha $
Tilting angle range	$ \alpha $	$\in [0^\circ, 35^\circ]$
Max tilting velocity	$\dot{\alpha} = -\hat{\alpha}$	$10^\circ/\text{s}$
Total mass	m	3.1 kg
Total inertia	$\mathbf{J}(i, i)_{i=1,2,3}$	$[0.089 \ 0.091 \ 0.164]^\top$ kg m ²
Max propeller spin	\bar{w}_i	102 Hz
Min propeller spin	\underline{w}_i	16 Hz
Max propeller force	\bar{f}_i	10 N
Max lift force	$f_{z,\text{max}}$	60 N
Max lateral force	$f_{xy,\text{max}}$	6 N
Thrust coefficient	c_f	$9.9\text{e-}4$ N/Hz ²
Drag-moment coefficient	c_f^T	$1.9\text{e-}2$ m
Propeller attitude	$\mathbf{R}_{A_i}^B$	$\mathbf{R}_z((i-1)\frac{\pi}{3})\mathbf{R}_x(\alpha_i)\mathbf{R}_y(\beta)$
i -th Propeller position	$\mathbf{p}_{A_i}^B$	$\mathbf{R}_z((i-1)\frac{\pi}{3})[\ell \ 0 \ 0]^\top$
Proportional gain (trasl.)	$\mathbf{K}_p(j, j)_{j=1,2,3}$	50, 50, 50
Integral gain (trasl.)	$\mathbf{K}_i(j, j)_{j=1,2,3}$	20, 20, 20
Derivative gain (trasl.)	$\mathbf{K}_v(j, j)_{j=1,2,3}$	14.14, 14.14, 14.14
Proportional gain (rot.)	$\mathbf{K}_R(j, j)_{j=1,2,3}$	15, 15, 6
Integral gain (rot.)	$\mathbf{K}_{R_i}(j, j)_{j=1,2,3}$	1, 1, 1
Derivative gain (rot.)	$\mathbf{K}_w(j, j)_{j=1,2,3}$	1.5, 1.5, 0.5

frames. This simplified model has been introduced in [25] – we will therefore only summarize it here.

The simplified FAST-Hex model is composed by a rigid body and six mass-free and orientable propellers. We define a world frame $\mathcal{F}_W = O_W, \{\mathbf{x}_W, \mathbf{y}_W, \mathbf{z}_W\}$ and a body frame $\mathcal{F}_B = O_B, \{\mathbf{x}_B, \mathbf{y}_B, \mathbf{z}_B\}$ that is rigidly attached to the FAST-Hex with O_B being the geometric center and the center of mass (CoM) of the system (see Fig. 1). The position of O_B is represented in \mathcal{F}_W by denoting $\mathbf{p}_B \in \mathbb{R}^3$ and the attitude of \mathcal{F}_B in \mathcal{F}_W is expressed by the rotation matrix $\mathbf{R}_B \in \text{SO}(3)$. The angular velocity of the body frame \mathcal{F}_B with respect to the world frame \mathcal{F}_W represented in \mathcal{F}_B is denoted with $\boldsymbol{\omega}_B \in \mathbb{R}^3$. The attitude kinematics of the body \mathbf{R}_B is then given by

$$\dot{\mathbf{R}}_B = \mathbf{R}_B[\boldsymbol{\omega}_B]_\times, \quad (2)$$

where $[\bullet]_\times \in \text{so}(3)$ represents any skew symmetric matrix associated to any vector $\bullet \in \mathbb{R}^3$.

Next, we introduce the six propeller frames $\mathcal{F}_{P_1}, \dots, \mathcal{F}_{P_6}$ with $\mathcal{F}_{P_i} = O_{P_i}, \{\mathbf{x}_{P_i}, \mathbf{y}_{P_i}, \mathbf{z}_{P_i}\}$. We denote with $\mathbf{e}_1, \mathbf{e}_2$, and \mathbf{e}_3 the three vectors of the canonical basis of \mathbb{R}^3 , and with \mathbf{R}_x and \mathbf{R}_z the two canonical rotation matrices in $\text{SO}(3)$. The orientation of the i -th propeller \mathcal{F}_{P_i} can now be expressed with respect to body frame \mathcal{F}_B by the rotation matrix

$$\mathbf{R}_{P_i}^B(\alpha) = \mathbf{R}_z\left((i-1)\frac{\pi}{3}\right)\mathbf{R}_x\left((-1)^{i-1}\alpha\right), \quad i = 1, \dots, 6 \quad (3)$$

where $\alpha \in [0^\circ, 35^\circ]$ is the *synchronized tilting angle* which is adjustable by using the single servomotor (see Fig. 1). The presence of $(-1)^{i-1}$ in (3) represents the effect that propellers with adjacent indexes are *tilting* in opposite directions, which guarantees the full actuation of the platform for $\alpha \in \mathcal{A} \setminus \{0\}$, see, e.g., [20], [28] for more details on the design of fully actuated platforms.

The vector originating from O_B to O_{P_i} , representing the position of the center of the i -th propeller, expressed in body frame \mathcal{F}_B , is

$$\mathbf{p}_{B,P_i}^B = l\mathbf{R}_z\left((i-1)\frac{\pi}{3}\right)\mathbf{e}_1, \quad \text{for } i = 1, \dots, 6 \quad (4)$$

with $l > 0$ being the distance from O_B to O_{P_i} . The six propellers are centered in O_{P_i} and spin with angular velocity $(-1)^{i-1}w_i\mathbf{z}_{P_i}$, where $(-1)^i$ models the property that propellers with adjacent indexes are designed to *spin* with opposite sign and therefore generate opposite drag torques. The six propeller spinning rates $w_i > 0$ are individually controllable.

In the following, we derive the dynamics of motion of the FAST-Hex platform which is actuated by changing the spinning velocity and synchronized orientation of the six propellers. While spinning, the propellers generate in a sufficient approximation a thrust force \mathbf{f}_i and a drag moment $\boldsymbol{\tau}_i$, applied in O_{P_i} and oriented along \mathbf{z}_{P_i} , which are expressed in \mathcal{F}_B as

$$\mathbf{f}_i^B(f_i, \alpha) = \mathbf{R}_{P_i}^B(\alpha)\mathbf{f}_i, \quad \text{for } i = 1, \dots, 6, \quad \text{and} \quad (5)$$

$$\boldsymbol{\tau}_i^B(f_i, \alpha) = (-1)^i c_f^T \mathbf{R}_{P_i}^B(\alpha)\mathbf{f}_i, \quad \text{for } i = 1, \dots, 6. \quad (6)$$

In (5) $c_f^T > 0$ is a constant parameter characterizing the relationship between the generated force and torque, depending on the physical parameters of the propeller. The scalar f_i is the intensity of the force produced by the propeller, which is related to the controllable spinning rate w_i by means of the quadratic relation

$$\mathbf{f}_i = f_i\mathbf{e}_3 = c_f w_i^2 \mathbf{e}_3, \quad (7)$$

where $c_f > 0$ is another propeller shape dependent constant parameter.

By summing all thrust forces, we find the total force applied to the FAST-Hex's CoM, expressed in world frame \mathcal{F}_W as

$$\mathbf{f}^W(\alpha, \mathbf{u}) = \mathbf{R}_B \sum_{i=1}^6 \mathbf{f}_i^B(f_i, \alpha) = \mathbf{R}_B \mathbf{F}_1(\alpha)\mathbf{u}, \quad (8)$$

where $\mathbf{u} = [f_1 \ f_2 \ f_3 \ f_4 \ f_5 \ f_6]^\top$ and $\mathbf{F}_1(\alpha) \in \mathbb{R}^{3 \times 6}$ is a suitable α -dependent matrix. For the case $\alpha = 0$ all propellers are collinear (as for a conventional hexarotor), then $\mathbf{F}_1(\alpha = 0) = [\mathbf{0}_6^\top \ \mathbf{0}_6^\top \ \mathbf{1}_6^\top]^\top$.

By adding all torque contributions, namely the drag moments (6) and the thrust contributions (5), we compute the total moment applied to the platform's CoM, with respect to O_B , and expressed in \mathcal{F}_B , as

$$\begin{aligned} \boldsymbol{\tau}^B(\alpha, \mathbf{u}) &= \sum_{i=1}^6 ((\mathbf{p}_{B,P_i}^B \times \mathbf{f}_i^B(f_i, \alpha)) + \boldsymbol{\tau}_i^B(f_i, \alpha)) \\ &= \mathbf{F}_2(\alpha)\mathbf{u}. \end{aligned} \quad (9)$$

The equations of motion of the aerial platform can be compactly expressed by using the Newton-Euler approach

$$\begin{bmatrix} m\ddot{\mathbf{p}}_B \\ \mathbf{J}\dot{\boldsymbol{\omega}}_B \end{bmatrix} = - \begin{bmatrix} mge_3 \\ \boldsymbol{\omega}_B \times \mathbf{J}\boldsymbol{\omega}_B \end{bmatrix} + \begin{bmatrix} \mathbf{f}^W \\ \boldsymbol{\tau}^B \end{bmatrix} \quad (10)$$

where $\mathbf{J} > 0$ represents the 3×3 inertia matrix of the rigid body with respect to O_B and expressed in \mathcal{F}_B , $m > 0$ represents the total mass of the FAST-Hex, and finally $g > 0$ is the gravitational acceleration.

Replacing (8) and (9) in (10) we obtain

$$\begin{bmatrix} m\ddot{\mathbf{p}}_B \\ \mathbf{J}\dot{\boldsymbol{\omega}}_B \end{bmatrix} = - \begin{bmatrix} mge_3 \\ \boldsymbol{\omega}_B \times \mathbf{J}\boldsymbol{\omega}_B \end{bmatrix} + \underbrace{\begin{bmatrix} \mathbf{R}_B \mathbf{F}_1(\alpha) \\ \mathbf{F}_2(\alpha) \end{bmatrix}}_{\mathbf{F}(\mathbf{R}_B, \alpha)} \mathbf{u}. \quad (11)$$

Finally, we will take propeller spinning rate saturations into account, which can be expressed as input limits as

$$\mathbf{u} \in \mathcal{U} = \{\mathbf{u} \in \mathbb{R}^6 \mid 0 \leq \underline{u} \leq f_i \leq \bar{u} \quad \forall i = 1 \dots 6\}. \quad (12)$$

where $\underline{u} \approx 0^+$ is the lower and \bar{u} are related to the upper spinning rate limit. While the upper spinning rate limit is caused by physical motor limitation, we additionally introduce a lower spinning rate limit as efficient propellers are optimized for a particular spinning direction and most propeller-motor controllers use an open loop propeller starting procedure with an undefined starting time making stopping undesirable [27].

A. Discussion on model simplifications

The presented, simplified FAST-Hex model neglects several properties of the actual system. In the following, we list the unmodeled properties and comment on their impact. While actively tilting the propellers, the gyroscopic effect causes a torque, perpendicular to the angular momentum of the propellers and the tilting direction. This gyroscopic effect is small due to the low mass of the propellers and the slow tilting velocity ($\bar{\alpha} = 10^\circ/\text{s}$) and we therefore neglect it. For the same reason, we ignore the multi-body dynamics between the actuated propellers and the main body. The actuation of the propellers causes a position change of the CoM and a change of the inertia matrix J of the main body in (10). These changes are as well small ($\Delta \mathbf{p}_{B,P_i}^B < 0.5\%$ in (9)). Additionally, we neglect the effects of the universal joints and the resulting minor position change of the propellers due to the actuation.

This work focuses on the mechanical design and the control of the FAST-Hex under a low velocity flight regime. We will therefore neglect aerodynamic effects such as the well-known first-order effects rotor drag, fuselage drag, and H-force, as these effects depend linearly on the vehicle's velocity and can therefore be neglected at small velocities [29].

We will demonstrate in the experimental results section (see Sec. V) that the controller presented in Sec. IV can sufficiently cope with these uncertainties.

B. Synchronized Tilting Angle: Efficiency vs. Full-Actuation

The FAST-Hex, with the tilting angle being $\alpha \in [0^\circ \ 35^\circ]$, has two structurally different configurations:

- 1) $\alpha = 0 \Rightarrow \text{rank}(\mathbf{F}(\mathbf{R}_B, \alpha = 0)) = 4$
- 2) $\alpha \in \mathcal{A} \setminus \{0\} \Rightarrow \text{rank}(\mathbf{F}(\mathbf{R}_B, \alpha)) = 6$.

In case the FAST-Hex would allow for $\alpha < 0^\circ$ the system would have an additional rank loss at $\alpha = -3.56^\circ$, in fact $\text{rank}(\mathbf{F}(\mathbf{R}_B, \alpha = -3.56^\circ)) = 5$ due to a yaw torque controllability loss [30]. We therefore restrict the tilting angle to positive values.

In configuration 1) all propellers of the FAST-Hex have collinear spinning axes. We will therefore call this configuration *Uni-Directional Thrust (UDT)* configuration opposing the *Multi-Directional Thrust (MDT)* in configuration 2). In UDT-configuration the system degenerates to an ordinary hexarotor platform. The internal forces in UDT-configuration are zero and only internal torques due to the drag moment appear. The internal torques due to drag moment are typically one order

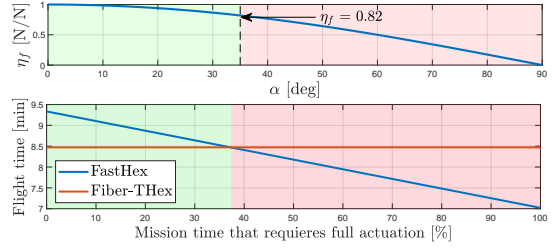


Fig. 5. Top: Nominal efficiency of the FAST-Hex depending on the tilting angle α based on the efficiency index presented in (13). The index is computed for horizontal hovering ($\mathbf{R}_B = I_{3 \times 3}$) condition. For the maximum tilting angle $\alpha = 35^\circ$ the efficiency drops to 0.82, meaning that 18% of the generated forces are “wasted” as internal forces. Bottom: Comparison of maximum flight time given the percentage of the mission that requires full actuation ($\alpha = 35^\circ$) for the FAST-Hex and the Fiber-THex [26], a fixed tilted hexarotor. If the mission profile requires less than 37% of the time full actuation (e.g., during taxi flights) then the FAST-Hex flight time is longer.

of magnitude less strong than the torques generated by the thrust moments and are therefore neglected in the following efficiency considerations.

We model the wasted (internal) force using the following index

$$\eta_f(\alpha, \mathbf{u}) = \frac{\|\sum_{i=1}^6 \mathbf{f}_i^B(f_i, \alpha)\|}{\sum_{i=1}^6 \|\mathbf{f}_i^B(f_i, \alpha)\|} = \frac{\|\sum_{i=1}^6 \mathbf{f}_i^B(f_i, \alpha)\|}{\sum_{i=1}^6 f_i} \in [0, 1] \quad (13)$$

that we call the *force efficiency* index. It is easy to check that $\eta_f(\alpha = 0, \mathbf{u}) = 1$ for any input \mathbf{u} , which corresponds to maximum efficiency. Hence the UDT-configuration is energetically very efficient. This comes with the drawback that the platform is under-actuated and a simultaneous tracking of fully independent $\mathbf{p}_r(t)$ and $\mathbf{R}_r(t)$ is impossible. The best choice left in this case is a control that selects a new reference orientation, denoted with $\mathbf{R}_d(t)$, that is compatible¹ with $\mathbf{p}_r(t)$ and is as close as possible to $\mathbf{R}_r(t)$ with respect to a certain criterion, as, e.g., possessing the same yaw angle of $\mathbf{R}_r(t)$, or the same projection of a certain axis on a certain plane. This approach is used, e.g., by the well established geometric control [31], whose rotational part is based on [32]. Almost global convergence is achieved without the singularities arising with the use of minimal orientation parametrizations.

In MDT-configuration the internal forces in hovering are greater than zero, which means that the system is wasting more energy than in UDT-configuration. The larger $|\alpha|$ the larger the internal forces. The efficiency index is strictly smaller than one, for all tilting angles but zero ($\eta_f(\alpha \in \mathcal{A} \setminus \{0\}, \mathbf{u}) < 1$). In particular, during horizontal hovering, when all the propellers are spinning at the same speed, producing the same force f , we have that $\eta_f(\alpha, f \mathbf{1}_{6 \times 1}) = \cos \alpha$. For horizontal hovering, we plot the efficiency index in Fig. 5-top for a changing tilting angle, showing that the efficiency drops to $\eta_f = 0.82$ for maximum tilting of $\alpha = 35^\circ$. If the platform is following a non-hovering trajectory then $\eta_f(\alpha, \mathbf{u})$ is in general different from $\cos \alpha$ and one has to use (13) to exactly compute it. On the other side in MDT-configurations the platform is fully-actuated, and the larger $|\alpha|$ the larger the volume of admissible total forces \mathbf{f}^W in (10), as it can be seen from Fig. 6. The simultaneous tracking of $\mathbf{p}_r(t)$ and $\mathbf{R}_r(t)$ becomes feasible

¹Compatibility is related to the well-known differential flatness property of collinear-rotor vehicles. In particular, the \mathbf{z}_B axis must be kept parallel to $\dot{\mathbf{p}}_r(t) + m\mathbf{g}\mathbf{e}_3$. The orientation about \mathbf{z}_B is instead not constrained by $\mathbf{p}_r(t)$.

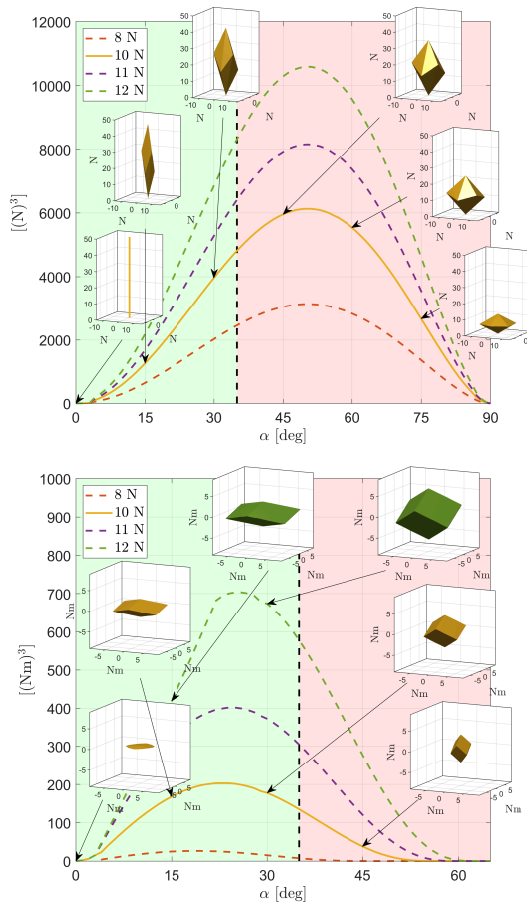


Fig. 6. Top: Volume of attainable total forces $\mathbf{R}_B^T \mathbf{f}^W(\alpha, \mathbf{u})$ corresponding to different values of α . The volumes are computed using (8), expressed in the body frame \mathcal{F}_B , and imposing $w_i \leq \bar{w}_i \forall i = 1, \dots, 6$ and $\boldsymbol{\tau}^B = \mathbf{0}$. The larger α (inside the feasible set) the larger the volume of the polyhedron. For $\alpha = 0$ the polyhedron degenerates to a single vector along the \mathbf{z}_B axis. The different lines represent different limits for the maximum rotor spinning velocity \bar{w}_i . Bottom: Volume of attainable total torques $\boldsymbol{\tau}^B(\alpha, \mathbf{u})$ corresponding to different values of α . The volumes are computed using (11), expressed in the body frame \mathcal{F}_B , and imposing $w_i \leq \bar{w}_i \forall i = 1, \dots, 6$ and $\mathbf{f}^B = [0 \ 0 \ mg]^T$.

as shown in [20], where a controller for this particular case is also proposed. We compared in Fig. 6 the influence of the tilting angle and the actuator limitations \bar{w}_i, w_i (see the limits in the inputs (12)) on the volume of admissible forces and torques depending on the tilting angle α . For computing the volume of admissible forces (top plot), we set the torques in (11) to $\boldsymbol{\tau}^B = \mathbf{0}$ Nm, while for computing the volume of admissible torques (bottom plot) we set the forces to obtain $\mathbf{f} = [0 \ 0 \ mg]^T$ N. The results of these plots as well drove the decision to limit the tilting angle $\bar{\alpha}$ to maximum 35° as the combined maximum torque and force volume is achieved at $\approx 35^\circ$.

Due to the fact that α is a slowly changeable parameter, the change of α is delegated to a high-level slow-rate controller/planner or to a human operator. The high-level controller can gently tune α while flying, thus continuously changing the platform between configuration 1) and any of the configurations of type 2) in order to adapt to the particular task being executed. For example, configuration 1) can be chosen when a pure horizontal hovering is requested, while a type 2) configuration

can be selected when hovering with non-zero roll and pitch is needed or to exert lateral forces in physical interaction tasks. Finally, we compared the feasible flight time of the FAST-Hex depending on the tilting angle α . Due the additional mechanical components enabling the tilting of the rotors, the FAST-Hex is heavier than a fixed tilted platform but more efficient while hovering or, more generally speaking if full actuation is not required. For this comparison we simulated the flight time of the FAST-Hex, depending on mission profiles requiring 0%-100% of the flight time full actuation and compared the flight time with the flight time of a fixed tilted hexarotor, namely the Fiber-THex an improved version of [26] (see Fig. 5-bottom). If the mission requires less than 37% of the flight time to be fully actuated the FAST-Hex is more energy efficient.

IV. FULL-POSE GEOMETRIC CONTROL WITH PRIORITIZED POSITION TRACKING

In this section, we present a control law for the six force inputs \mathbf{u} in (12) that lets \mathbf{p}_B and \mathbf{R}_B track at best an arbitrary full-pose reference trajectory $(\mathbf{p}_r(t), \mathbf{R}_r(t)) : \mathbb{R} \rightarrow \mathbb{R}^3 \times \text{SO}(3)$. The time-varying parameter α is given to the controller. By decoupling the control of α and \mathbf{u} , we make the control law directly applicable for a broad spectrum of aerial vehicles beyond the scope of the FAST-Hex.

The most obvious approach to control the FAST-Hex would be to use the geometric controller presented in [31] while in configuration 1) and the fully-actuated controller [20] while in configuration 2). The first drawback of this approach concerns the challenges that might arise from switching between two controllers, and the second is an ill-conditioned computation of $\mathbf{F}(\mathbf{R}_B, \alpha)^{-1}$ (used in [20]) for $\alpha \rightarrow 0$. A possible solution to the ill-conditioned inversion would be to use the geometric controller [31] for even small angles of $|\alpha|$, which would require abandoning full-pose tracking for small values of α . However, it might be actually desirable to drive the FAST-Hex with a small α angle in order to find a trade-off between full actuation and minimization of wasted internal forces.

Therefore, we suggest using a control that works seamlessly in both configurations, an extension of the under-actuated geometric control [31] for fully actuated platforms. The desired behavior of a platform driven by the controller will then be:

- The larger α the more the platform can realize an arbitrary force vector and track simultaneously a position and orientation trajectory. The FAST-Hex becomes gradually fully actuated.
- The smaller α the more the output of the control law resembles [31]. In other words, when $|\alpha|$ decreases the FAST-Hex becomes gradually under-actuated, *i.e.*, it still keeps a good tracking of the reference position but it becomes progressively unable to independently track also a generic reference orientation.

The implemented controller is an improvement of the full-pose geometric controller with prioritised position tracking described in [25] which is composed by an inner *attitude controller* and an outer *position controller*. The controllers are then cascaded by a *wrench mapper* which computes the actuators set-point \mathbf{u} according to the desired control force

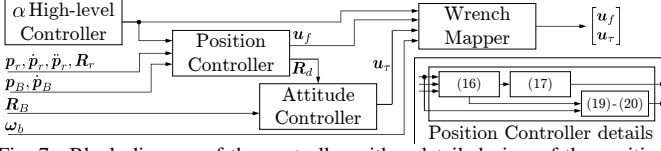


Fig. 7. Block diagram of the controller with a detailed view of the position controller including references to equations.

$\mathbf{u}_f \in \mathbb{R}^3$ and moment $\mathbf{u}_r \in \mathbb{R}^3$ provided by the position and attitude controllers, respectively. An overview of the controller is depicted in Fig. 7. In the following, the three components are described in detail.

A. Position control

The position controller takes as input the full-pose reference trajectory ($\mathbf{p}_r, \dot{\mathbf{p}}_r, \ddot{\mathbf{p}}_r \in \mathbb{R}^3$ and $\mathbf{R}_r = [\mathbf{b}_{1r} \ \mathbf{b}_{2r} \ \mathbf{b}_{3r}] \in \text{SO}(3)$), the measured position \mathbf{p}_B , the measured linear velocity $\dot{\mathbf{p}}_B$ and the measured attitude \mathbf{R}_B . It produces as outputs the desired control force \mathbf{u}_f and the desired orientation $\mathbf{R}_d \in \text{SO}(3)$, which are both fed as inputs to the attitude controller. We shall describe the position controller in detail next.

Given the considered inputs we define the position and velocity tracking errors as follows:

$$\mathbf{e}_p = \mathbf{p}_B - \mathbf{p}_r, \quad \mathbf{e}_v = \dot{\mathbf{e}}_p = \dot{\mathbf{p}}_B - \dot{\mathbf{p}}_r. \quad (14)$$

It is then possible to define the integral position tracking error as

$$\mathbf{e}_{pi} = \int_0^t \mathbf{e}_p d\tau. \quad (15)$$

The reference force vector is then computed as

$$\mathbf{f}_r = m(\ddot{\mathbf{p}}_r + g\mathbf{e}_3) - \mathbf{K}_p \mathbf{e}_p - \mathbf{K}_{pi} \mathbf{e}_{pi} - \mathbf{K}_v \mathbf{e}_v, \quad (16)$$

where $\mathbf{K}_p, \mathbf{K}_{pi}, \mathbf{K}_v \in \mathbb{R}^{3 \times 3}$ are positive diagonal gain matrices.

The maximum lateral force of the FAST-Hex increases nonlinearly with the tilting angle α . We can express the lateral force bound r_{xy} as a function of α . To find the function $r_{xy}(\alpha)$ we numerically computed the maximum lateral force at hovering assuming zero desired torque (Fig. 8-left). Since the sets of admissible lateral forces have a hexagonal shape, we decided to consider the circle inscribed in each hexagon as a lateral force bound. To exploit r_{xy} as a function of α a Least Squares (LS) approach has been used to interpolate the obtained values with a second degree polynomial. The polynomial has been scaled down with a tunable gain leading to a more conservative lateral force bound. Finally, to prevent extreme propeller spinning velocities due an ill-conditioned pseudo inverse for very small values of α (see (24)), a dead-zone in the proximity of $\alpha = 0$ has been introduced (see Figure 8-right). We can now define the lateral force bound as

$$r_{xy} = \begin{cases} 0, & \text{if } \alpha \leq k_{\text{dead}} \\ (\alpha - k_{\text{dead}})^2, & \text{elseif } k_{\text{dead}} \leq \alpha \leq k_{\text{int}} \\ k_{\text{tune}} * (k_1 \alpha^2 + k_2 \alpha), & \text{otherwise,} \end{cases} \quad (17)$$

where $k_{\text{dead}} = 3.5^\circ$ is the gain for the dead-zone, k_{int} is the intersection point between the two curves, $k_{\text{tune}} = 0.85$ is the tunable gain and $k_1 = -1.65$ and $k_2 = 14.40$ are the coefficients of the polynomial.

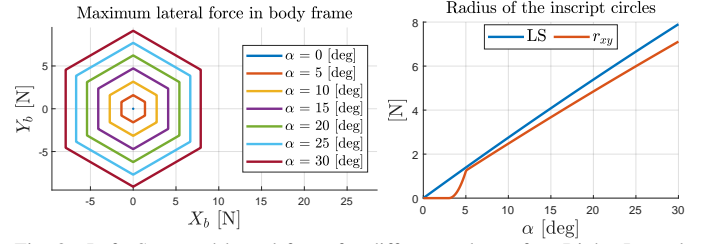


Fig. 8. Left: Saturated lateral force for different values of α . Right: Lateral force saturation function.

Algorithm 1: Computation of \mathbf{R}_d via bisection method

Input : $\mathbf{b}_{3r}, \mathbf{f}_r, r_{xy}(\alpha)$
Data: n (number of iterations \propto solution accuracy)
1 $\theta_{max} \leftarrow \arcsin\left(\frac{\|\mathbf{b}_{3r} \times \mathbf{f}_r\|}{\|\mathbf{f}_r\|}\right)$, $\theta \leftarrow \frac{\theta_{max}}{2}$, $\mathbf{k} \leftarrow \frac{\mathbf{b}_{3r} \times \mathbf{f}_r}{\|\mathbf{b}_{3r} \times \mathbf{f}_r\|}$;
2 **for** $i = 1$ **to** n **do**
3 $\mathbf{b}_{3d} \leftarrow \mathbf{b}_{3r} c_\theta + (\mathbf{k} \times \mathbf{b}_{3r}) s_\theta + \mathbf{k} (\mathbf{k} \cdot \mathbf{b}_{3r}) (1 - c_\theta)$;
4 **if** $\mathbf{f}_r^\top \mathbf{b}_{3d} \geq \sqrt{\|\mathbf{f}_r\|^2 - r_{xy}^2(\alpha)}$ **then** $\theta \leftarrow \theta - \frac{\theta_{max}}{2} \frac{1}{2^i}$;
5 **else** $\theta \leftarrow \theta + \frac{\theta_{max}}{2} \frac{1}{2^i}$;
6 **return** θ

The force vector is then rotated from inertial to body frame to obtain the control force. We saturate the control force assuming a cylindrical bound [26] (with cylinder radius $r_{xy}(\alpha)$) considering the current maximum lateral forces and obtain the desired control force as

$$\mathbf{u}_f = \begin{bmatrix} \text{sat}_{r_{xy}}(u_{f_1}) \\ \text{sat}_{r_{xy}}(u_{f_2}) \\ u_{f_3} \end{bmatrix} = \begin{bmatrix} \text{sat}_{r_{xy}}(\mathbf{u}_{f_{1,2}}) \\ u_{f_3} \end{bmatrix} = \text{sat}(\mathbf{R}_B^\top \mathbf{f}_r)$$

with

$$\text{sat}_{r_{xy}} \begin{pmatrix} u_{f_1} \\ u_{f_2} \end{pmatrix} = \begin{cases} \begin{bmatrix} \mathbf{u}_{f_{1,2}} \\ \frac{u_{f_1} \cdot r_{xy}}{\|\mathbf{u}_{f_{1,2}}\|} \\ \frac{u_{f_2} \cdot r_{xy}}{\|\mathbf{u}_{f_{1,2}}\|} \end{bmatrix}, & \text{if } u_{f_1}^2 + u_{f_2}^2 \leq r_{xy}^2(\alpha) \\ \begin{bmatrix} \frac{u_{f_1} \cdot r_{xy}}{\|\mathbf{u}_{f_{1,2}}\|} \\ \frac{u_{f_2} \cdot r_{xy}}{\|\mathbf{u}_{f_{1,2}}\|} \end{bmatrix}, & \text{otherwise.} \end{cases} \quad (18)$$

We now seek to find a desired orientation \mathbf{R}_d that is as close as possible to the reference orientation \mathbf{R}_r but allows to implement the reference force \mathbf{f}_r without violating the lateral force bound r_{xy} . This can be achieved by minimizing the following cost function

$$\min_{\mathbf{f}_r^\top \mathbf{b}_{3d}(\theta) \geq \sqrt{\|\mathbf{f}_r\|^2 - r_{xy}^2(\theta)}} -\mathbf{b}_{3r}^\top \mathbf{b}_{3d}(\theta). \quad (19)$$

where \mathbf{b}_{3r} and \mathbf{b}_{3d} are the third column vectors of $\mathbf{R}_r = [\mathbf{b}_{1r} \ \mathbf{b}_{2r} \ \mathbf{b}_{3r}]$ and $\mathbf{R}_d = [\mathbf{b}_{1r} \ \mathbf{b}_{2r} \ \mathbf{b}_{3d}]$ and $\theta = \arccos \frac{\mathbf{b}_{3r} \cdot \mathbf{b}_{3d}}{\|\mathbf{b}_{3r}\| \|\mathbf{b}_{3d}\|}$. We can find the vector \mathbf{b}_{3d} by using Rodrigues' rotation formula as $\mathbf{b}_{3d} = \mathbf{b}_{3r} c_\theta + (\mathbf{k} \times \mathbf{b}_{3r}) s_\theta + \mathbf{k} (\mathbf{k} \cdot \mathbf{b}_{3r}) (1 - c_\theta)$ [33], where $\mathbf{k} = \frac{\mathbf{b}_{3r} \times \mathbf{f}_r}{\|\mathbf{b}_{3r} \times \mathbf{f}_r\|}$, while the minimization problem in (19) can be solved efficiently by using a bisection search method as described in Alg. 1. Finally, it is possible to compute the desired orientation as

$$\mathbf{R}_d = \begin{bmatrix} \underbrace{(\mathbf{b}_{3d} \times \mathbf{b}_{1r}) \times \mathbf{b}_{3d}}_{\mathbf{b}_{1d}} & \underbrace{\mathbf{b}_{3d} \times \mathbf{b}_{1r}}_{\mathbf{b}_{2d}} & \mathbf{b}_{3d} \end{bmatrix}. \quad (20)$$

B. Attitude control

The attitude controller takes as input the desired orientation computed from the position controller (\mathbf{R}_d), the measured orientation (\mathbf{R}_B), and the measured angular velocity ($\boldsymbol{\omega}_B$) to compute the desired control torque (\mathbf{u}_τ).

The desired control torque is computed as

$$\mathbf{u}_\tau = \boldsymbol{\omega}_B \times \mathbf{J}\boldsymbol{\omega}_B - \mathbf{K}_R \mathbf{e}_R - \mathbf{K}_{Ri} \mathbf{e}_{Ri} - \mathbf{K}_\omega \boldsymbol{\omega}_B, \quad (21)$$

where \mathbf{K}_R , \mathbf{K}_{Ri} , $\mathbf{K}_\omega \in \mathbb{R}^{3 \times 3}$ are positive diagonal gain matrices and \mathbf{e}_R is the orientation tracking error defined as

$$\mathbf{e}_R = \frac{1}{2} \left(\mathbf{R}_d^\top \mathbf{R}_B - \mathbf{R}_B^\top \mathbf{R}_d \right)^\vee, \quad (22)$$

with \bullet^\vee which is the vee map from $\text{SO}(3)$ to \mathbb{R}^3 and \mathbf{e}_{Ri} the integral orientation tracking error computed as

$$\mathbf{e}_{Ri} = \int_0^t \mathbf{e}_R d\tau. \quad (23)$$

C. Wrench mapper

The wrench mapper takes as input the desired control force in (18) and moment in (21) provided by the position and attitude controller, respectively, and computes a feasible \mathbf{u} through the nonlinear map

$$\mathbf{u} = \mathbf{F}(\alpha)^\dagger \begin{bmatrix} \mathbf{u}_f \\ \mathbf{u}_\tau \end{bmatrix}, \quad (24)$$

where $\mathbf{F}(\alpha) \in \mathbb{R}^{6 \times 6} = [\mathbf{F}_1 \ \mathbf{F}_2]^\top$ is the allocation map in (11) without the rotation matrix \mathbf{R}_b . Since the structural properties of the allocation map $\mathbf{F}(\alpha)$ change with the tilting angle α (*i.e.*, with $\alpha = 0$ the allocation map becomes singular or it may be ill-conditioned if $\alpha \approx 0$) the computation of the wrench mapper is not trivial and the use of a simple inversion is not possible. We therefore use in (24) the Moore-Penrose pseudo-inverse (\dagger) to allocate \mathbf{u} .

V. EXPERIMENTAL VALIDATION

A. Experimental setup

The physical and control parameters and controller gains of the FAST-Hex are reported in Tab. I. In particular, the controller gains have been initially tuned on MATLAB/Simulink environment by means of a ad-hoc simulator and eventually fine-tuned on the real flying platform.

The controller has been developed in Matlab-Simulink and runs at a frequency of 500 Hz on a stationary ground station. The ground station is connected with the FAST-Hex with a serial cable. This setup has been selected for fast development and testing of the controller but could be ported with some straightforward effort to an on-board system as the computational demand of the controller is negligible. Therefore, we would expect an increased performance as an on-board control would benefit from a possibly higher control frequency, no communication delay and no disturbance from the hanging serial cables. For some experiments we replaced the battery by an external power supply. The following presented experiments are therefore a baseline on which the system could be improved.

On-board the FAST-Hex an inertial measurement unit provides acceleration and angular rate at 500 Hz. An external

marker-based motion capture (MoCap) system provides with sub-centimeter accuracy the pose measurements of the aerial robot at 100 Hz. The IMU and the pose measurements are fused via an Unscented Kalman Filter state estimator to obtain full state estimates at control frequency rate (500 Hz). The external MoCap system could as well be replaced by an on-board camera and a Perspective-n-Point algorithm to estimate the robot's pose. However, we purposefully neglected this possibility to evaluate the FAST-Hex and its controller without additional influences of the particular perception system.

We report two sets of experiments in this paper. In the first set (see Sec. V-B) we demonstrate basic hovering capabilities during reconfiguration of the tilting angle. In the second set (see Sec. V-C) we present dynamic trajectory tracking for two kinds of trajectories, sinusoidal attitude tracking with a fixed position and sinusoidal position tracking with a fixed attitude, both with a time varying tilting angle. An additional experiment, comparing the robustness of the platform to external force disturbance during full- and under-actuation, can be found in the attached technical report. We will present several plots in the following figures. In single column figures we refer to the plots from top to bottom with increasing numbers. In double column figures we refer to the plots from top to bottom in the first column and then from top to bottom in the second column with increasing numbers. For an easier understanding, we highlighted in all plots with a bright red background while the FAST-Hex is in UDT-configuration and with a bright green background as soon as the platform is in MDT-configuration. In order to better appreciate the discussed experiments and their results, we suggest the reader to watch the attached videos.

B. Experiment 1: Static Hovering

In this experiment, the FAST-Hex is commanded to hover statically, *i.e.*, to resist the gravitational force while maintaining a constant position $\mathbf{p}_r = [-0.14 \ -0.05 \ 1]^\top$ m and a horizontal orientation, *i.e.*, $\mathbf{R}_r = \mathbf{I}_3$. Additionally, the reference angle α_r for the synchronized tilting angle of the actuators has a rectangular profile between the values $\alpha_1 = 0^\circ$ and $\alpha_2 = 30^\circ$ (see first, third and seventh plot in Fig. 9). As a consequence, the robot switches its configuration from UDT to MDT and back.

The goal of the experiment is to demonstrate the controller's capability to safely change between the two configurations UDT and MDT and assess the controller's robustness with respect to the unmodeled effects discussed in Sec. III-A.

Observing the position and attitude tracking, there are only small tracking errors (plot 2 and 5 in Fig. 9) during the configuration transition. Generally, the overall mean position tracking error is $\|\mathbf{e}_p\| = 8.7$ mm, with a significantly smaller tracking error while being in MDT configuration ($\|\mathbf{e}_p^{\text{MDT}}\| = 5.5$ mm vs. $\|\mathbf{e}_p^{\text{UDT}}\| = 6.7$ mm - we ignored the initial time after a configuration change as the transition causes a short increase of the tracking error). The overall mean attitude tracking error is as well small ($\bar{e}_\phi = 0.84^\circ$, $\bar{e}_\theta = 0.92^\circ$, $\bar{e}_\psi = 1.10^\circ$) with again a significantly smaller mean error for roll and pitch during MDT configuration ($\bar{e}_\phi^{\text{MDT}} = 0.35^\circ$, $\bar{e}_\theta^{\text{MDT}} = 0.35^\circ$ vs. $\bar{e}_\phi^{\text{UDT}} = 0.54^\circ$, $\bar{e}_\theta^{\text{UDT}} = 0.45^\circ$). However, the yaw tracking error

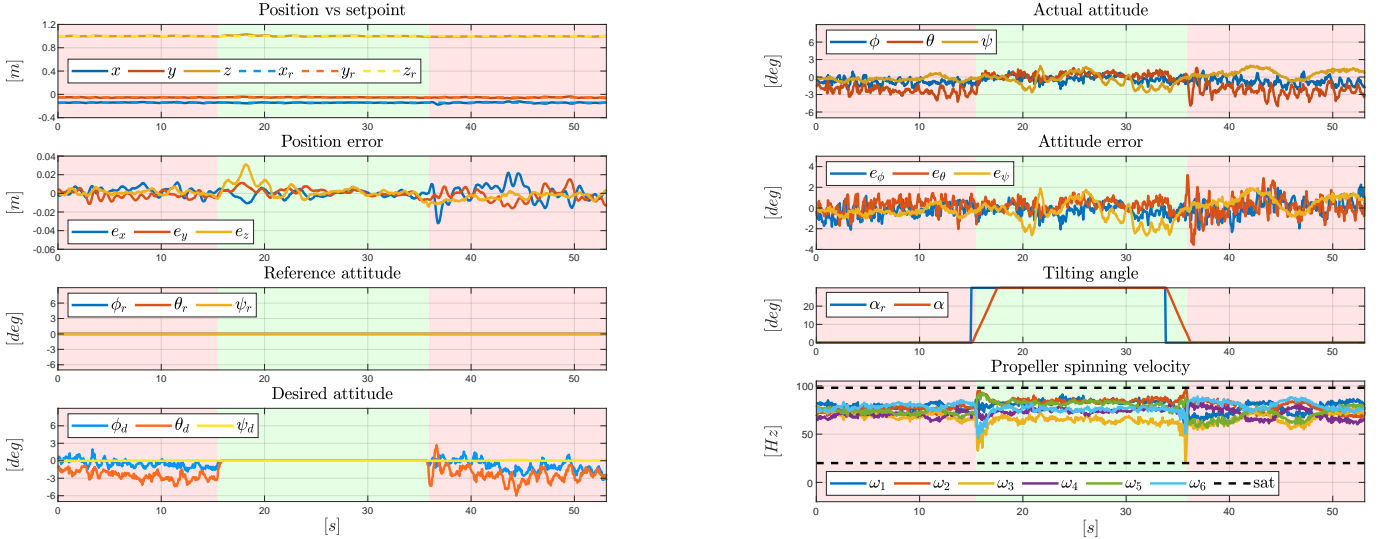


Fig. 9. Plots of Experiment 1 - left column from top to bottom: 1) Actual vs reference position; 2) Position tracking error; 3) Reference attitude depicted in Euler angles; 4) Desired attitude depicted in Euler angles. Right column from top to bottom: 5) Actual attitude depicted in Euler angles; 6) Attitude tracking error; 7) Reference and actual tilting angle; 8) Actual propeller spinning velocity. While the FAST-Hex is under-actuated the plots are highlighted in red. On the other hand, during full actuation the plots are highlighted in green.

is larger ($\overline{e_{\psi}^{\text{MDT}}} = 0.76^\circ$ vs. $\overline{e_{\psi}^{\text{UDT}}} = 0.37^\circ$). This is due to small misalignments of the propellers, whose effects on the tracking performance are more evident when the control authority on the yaw moment is larger, *i.e.*, when $\alpha \gg 0$.

The plots of the reference \mathbf{R}_r and the desired attitude \mathbf{R}_d (see Fig. 9 - plot 3 and 4) induce interesting insights on the behavior of the inner attitude control loop. Comparing the third and the fourth plot, it becomes clear that the control algorithm is required to re-compute the desired orientation for the system while being in UDT configuration. Indeed, when the system is under-actuated the only feasible reference is the one given by the well-known flatness property [29]. In this case, the desired orientation is continuously regulated to correct position errors. The non-exact zero mean for ϕ_d and θ_d is due to parameters mismatches between the model and the real system, especially of those associated with the orientation of the actuators, and to external disturbances like the one induced by the serial cable. Conversely, as soon as the angle α is large enough the robot can exert lateral forces without the need of re-orient itself and so the desired attitude can be constantly flat.

Finally, we would like to discuss the desired spinning velocities for the rotors computed by the pose controller depicted in the sixth plot. As it can be appreciated, the signals remain bounded by their limits, which demonstrate the controller ability to comply with the actuator bounds. Furthermore, it is worthwhile to observe the peaks in the actuator commands during the changes of configuration, due to the reduced control authority during the under/fully actuated transition phase that is also the cause of the increase in the position tracking error.

C. Experiment 2: Dynamic Trajectory Tracking

In this set of experiments, we command the FAST-Hex to track two trajectories with independent position and orientation profile, which is unfeasible for standard collinear multirotor platforms. The goal of these two experimental sets is to

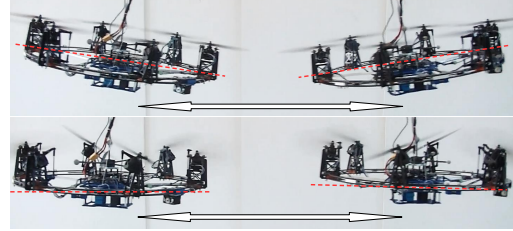


Fig. 10. Time-lapse pictures of the FAST-Hex during Experiment 2-a: Top: While being in UDT-configuration (tilting angle is zero) the platform cannot generate horizontal forces and the controller needs to adapt the attitude trajectory to be able to track the position trajectory. Bottom: With tilted propellers, the FAST-Hex is able to generate lateral forces and the platform can track independent position and attitude trajectories (depending on the actuation constraints) and therefore remain horizontal while traversing laterally.

demonstrate how the pose tracking of the controller is fulfilled when the tilting angle is changed over time.

1) Sinusoidal translation with constant horizontal attitude:

In this experiment, we aim at tracking a translational sine-wave trajectory while maintaining a horizontal attitude ($\mathbf{R}_r = \mathbf{I}_3$). The amplitude of the translational sine-wave is 1.2 m with a peak velocity of $\hat{p}_{x_r} = 1$ m/s and a peak acceleration of $\hat{p}_{x_r} = 1.67$ m/s² (see Fig. 11 - 1). The tilting angle α is increased over time from 0° to 30° (see Fig. 11 - last plot). A photograph of the FAST-Hex while tracking this trajectory in the two different configurations is provided in Fig. 10.

From plots 3 and 4 of Fig. 11 it becomes clear that the controller has to significantly alter the reference trajectory to output a trackable desired trajectory while the platform is under-actuated (until $t \approx 20$ s). During this initial phase of the experiment, the maximum lateral force f_{xy} is zero (see plot 7) making the attitude dynamics fully coupled with the position dynamics. As soon as the lateral force f_{xy} is not zero but increases over time, the desired trajectory gradually approaches the reference trajectory. It is interesting to point out that even with fully tilted propellers, the lateral forces required to track a fully horizontal trajectory would violate the maximum spinning velocity of the propellers (see plot 6).

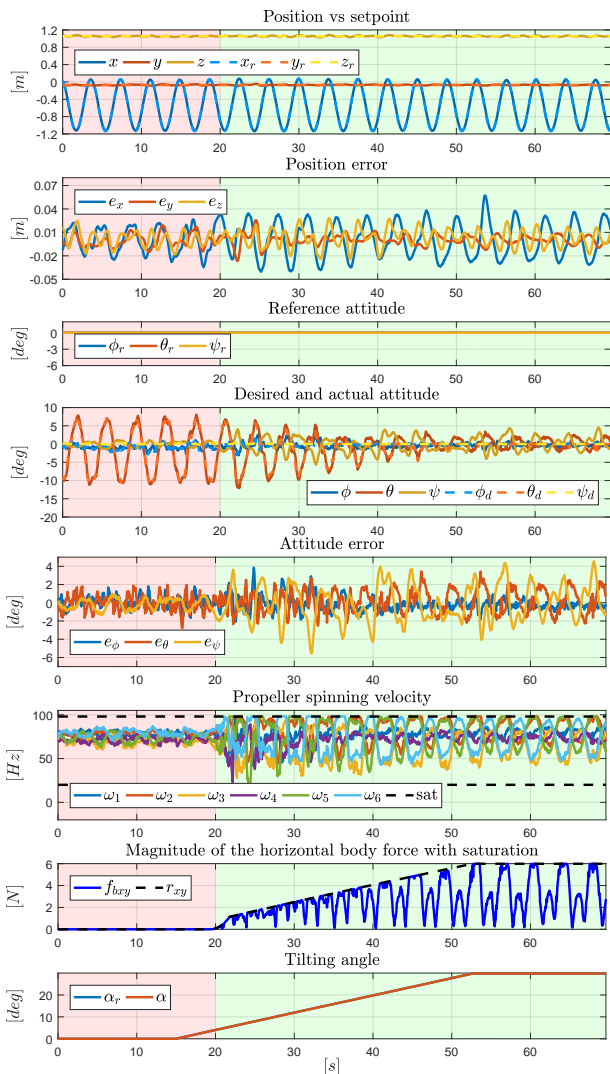


Fig. 11. Plots of Experiment 2-a - from top to bottom. 1) Actual vs reference position; 2) Position tracking error; 3) Reference attitude depicted in Euler angles; 4) Desired and actual attitude depicted in Euler angles; 5) Attitude tracking error; 6) Actual propeller spinning velocity; 7) Maximum and actual lateral force; 8) Reference and actual tilting angle. While the FAST-Hex is under-actuated, the plots are highlighted in red, during full actuation, the plots are highlighted in green.

Therefore, the desired trajectory diverges slightly from the reference trajectory at the peaks of the translation.

2) *Hovering with sinusoidal rolling*: In the second dynamic reference motion, the position trajectory is constant with $\mathbf{p}_r = [-0.08 \ -0.03 \ 1]^T$ m, while the roll angle follows a sine-wave with a peak angle of 6° and a frequency of about 0.1 Hz. The pitch and yaw angles remain constant at 0° . The plots related to this trajectory, which is unfeasible for a UDT vehicle, are depicted in Fig. 12.

The reference tilting angle is increased linearly from $\alpha = 0^\circ$ to $\alpha = 30^\circ$, as in the previous experiment (see last plot in Fig. 12). The controller is therefore required to adapt the reference trajectory into a trackable desired trajectory.

The static reference \mathbf{p}_r and actual body position \mathbf{p}_B are depicted in the first plot in Fig. 12. The position tracking error remains small with mean position error of $\|\mathbf{e}_p\| = 10.4$ mm. The position error does not significantly change between the configurations. A standard collinear multirotor is not able to

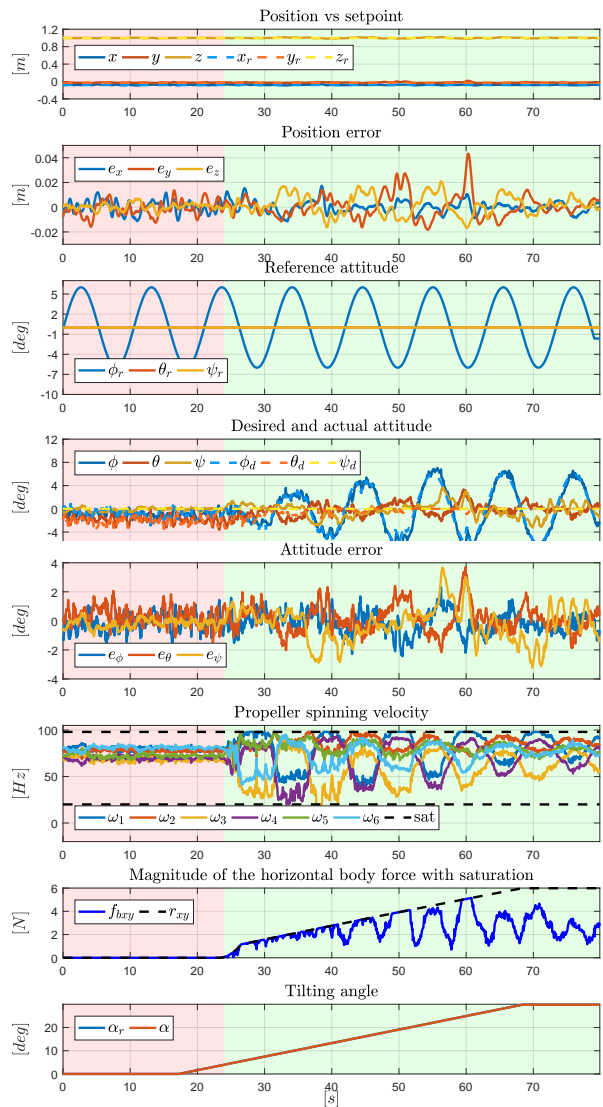


Fig. 12. Plots of Experiment 2-b - from top to bottom. 1) Actual vs reference position; 2) Position tracking error; 3) Reference attitude depicted in Euler angles; 4) Desired and actual attitude depicted in Euler angles; 5) Attitude tracking error; 6) Actual propeller spinning velocity; 7) Maximum and actual lateral force; 8) Reference and actual tilting angle. While the FAST-Hex is under-actuated, the plots are highlighted in red, during full actuation, the plots are highlighted in green.

track a trajectory for roll and pitch while remaining at a fixed location, as multi-directional forces would need to be applied. Therefore, the FAST-Hex cannot track the reference attitude trajectory initially (see Fig. 12 - plot 4). As a consequence, the controller outputs a desired trajectory that is basically constant and horizontal. As soon as the feasible horizontal body force is large enough (see plot 7) thanks to an increasing tilting angle, the FAST-Hex gradually starts to track the reference attitude trajectory. Starting from $t \approx 60$ s, the tilting angle is large enough to fully track the reference attitude. The lateral forces required to track the desired rolling motion can now be completely generated by the propellers (see plot 6 and 7).

VI. CONCLUSION AND FUTURE WORK

In this paper, we presented a novel morphing hexarotor platform - the FAST-Hex. The careful integration of a single additional actuator allows the platform to efficiently transition

from under-actuation to full-actuation. We presented and discussed the hardware implementation, and the control framework that allows to drive the platform seamlessly in both conditions, while prioritizing position tracking over attitude tracking if the actuation limitations cannot be met otherwise.

We presented an extensive set of flight experiments, showing general trajectory tracking performance in static and dynamic flight regimes in both configurations. Furthermore, we discussed the benefits of morphing aerial platforms under the effect of external force disturbances.

REFERENCES

- [1] D. Falanga, K. Kleber, S. Mintchev, D. Floreano, and D. Scaramuzza, "The foldable drone: A morphing quadrotor that can squeeze and fly," *IEEE Robotics and Automation Letters*, vol. 4, no. 2, pp. 209–216, 2018.
- [2] V. Riviere, A. Manecy, and S. Viollet, "Agile robotic fliers: A morphing-based approach," *Soft robotics*, vol. 5, no. 5, pp. 541–553, 2018.
- [3] D. Pastor, J. Izraelevitz, P. Nadan, A. Bouman, J. Burdick, and B. Kennedy, "Design of a ballistically-launched foldable multirotor," 2019.
- [4] M. Zhao, K. Kawasaki, X. Chen, S. Noda, K. Okada, and M. Inaba, "Whole-body aerial manipulation by transformable multirotor with two-dimensional multilinks," in *2017 IEEE International Conference on Robotics and Automation (ICRA)*. IEEE, 2017, pp. 5175–5182.
- [5] M. Zhao, T. Anzai, F. Shi, X. Chen, K. Okada, and M. Inaba, "Design, modeling, and control of an aerial robot dragon: A dual-rotor-embedded multilink robot with the ability of multi-degree-of-freedom aerial transformation," *IEEE Robotics and Automation Letters*, vol. 3, no. 2, pp. 1176–1183, 2018.
- [6] M. Zhao, F. Shi, T. Anzai, K. Okada, and M. Inaba, "Online motion planning for deforming maneuvering and manipulation by multilinked aerial robot based on differential kinematics," *IEEE Robotics and Automation Letters*, vol. 5, no. 2, pp. 1602–1609, 2020.
- [7] M. Kulkarni, H. Nguyen, and K. Alexis, "The reconfigurable aerial robotic chain: Shape and motion planning," 2019.
- [8] M. Nigro, F. Pierri, and F. Caccavale, "Preliminary design, modeling and control of a fully actuated quadrotor uav," in *2019 International Conference on Unmanned Aircraft Systems (ICUAS)*, June 2019, pp. 1108–1116.
- [9] M. Ryll, H. H. Bühlhoff, and P. Robuffo Giordano, "Modeling and control of a quadrotor UAV with tilting propellers," in *2012 IEEE Int. Conf. on Robotics and Automation*, St. Paul, MN, May 2012, pp. 4606–4613.
- [10] M. Ryll, H. H. Bühlhoff, and P. Robuffo Giordano, "First flight tests for a quadrotor UAV with tilting propellers," in *2013 IEEE Int. Conf. on Robotics and Automation*, Karlsruhe, Germany, May 2013, pp. 295–302.
- [11] M. Kamel, S. Verling, O. Elkhatib, C. Sprecher, P. Wulkop, Z. Taylor, R. Siegart, and I. Gilitschenski, "The voliro omniorientational hexacopter: An agile and maneuverable tiltable-rotor aerial vehicle," *IEEE Robotics & Automation Magazine*, vol. 25, no. 4, pp. 34–44, 2018.
- [12] D. Invernizzi, M. Giurato, P. Gattazzo, and M. Lovera, "Full pose tracking for a tilt-arm quadrotor UAV," in *2018 IEEE Conference on Control Technology and Applications (CCTA)*. IEEE, 2018, pp. 159–164.
- [13] R. Voyles and G. Jiang, "A nonparallel hexrotor UAV with faster response to disturbances for precision position keeping," in *2014 IEEE Int. Symp. on Safety, Security and Rescue Robotics*, West Lafayette, IN, Oct. 2014, pp. 1–5.
- [14] P. Segui-Gasco, Y. Al-Rihani, H.-S. Shin, and A. Savvaris, "A novel actuation concept for a multi rotor UAV," in *2013 Int. Conf. on Unmanned Aircraft Systems*, Atlanta, GA, May 2013, pp. 373–382.
- [15] D. Invernizzi and M. Lovera, "Trajectory tracking control of thrust-vectoring UAVs," *Automatica*, vol. 95, pp. 180–186, 2018.
- [16] D. Invernizzi, M. Lovera, and L. Zaccarian, "Dynamic attitude planning for trajectory tracking in thrust-vectoring uavs," *IEEE Transactions on Automatic Control*, vol. 65, no. 1, pp. 180–186, 2020.
- [17] B. Crowther, A. Lanzon, M. Maya-Gonzalez, and D. Langkamp, "Kinematic analysis and control design for a nonplanar multirotor vehicle," *AIAA Journal of Guidance, Control, and Dynamics*, vol. 34, no. 4, pp. 1157–1171, 2011.
- [18] M.-D. Hua, T. Hamel, P. Morin, and C. Samson, "Control of VTOL vehicles with thrust-tilting augmentation," *Automatica*, vol. 52, pp. 1–7, 2015.
- [19] M. Ryll, H. H. Bühlhoff, and P. Robuffo Giordano, "A novel overactuated quadrotor unmanned aerial vehicle: modeling, control, and experimental validation," *IEEE Trans. on Control Systems Technology*, vol. 23, no. 2, pp. 540–556, 2015.
- [20] S. Rajappa, M. Ryll, H. H. Bühlhoff, and A. Franchi, "Modeling, control and design optimization for a fully-actuated hexarotor aerial vehicle with tilted propellers," in *2015 IEEE Int. Conf. on Robotics and Automation*, Seattle, WA, May 2015, pp. 4006–4013.
- [21] Y. Long, L. Wang, and D. J. Cappelleri, "Modeling and global trajectory tracking control for an over-actuated MAV," *Advanced Robotics*, vol. 28, no. 3, pp. 145–155, 2013.
- [22] A. Oosedo, S. Abiko, S. Narasaki, A. Kuno, A. Konno, and M. Uchiyama, "Flight control systems of a quad tilt rotor unmanned aerial vehicle for a large attitude change," in *2015 IEEE Int. Conf. on Robotics and Automation*, Seattle, WA, May 2015, pp. 2326–2331.
- [23] D. Brescianini and R. D'Andrea, "Design, modeling and control of an omnidirectional aerial vehicle," in *2016 IEEE Int. Conf. on Robotics and Automation*, Stockholm, Sweden, May 2016, pp. 3261–3266.
- [24] M. Ryll, G. Muscio, F. Pierri, E. Cataldi, G. Antonelli, F. Caccavale, D. Bicego, and A. Franchi, "6D interaction control with aerial robots: The flying end-effector paradigm," *The International Journal of Robotics Research*, vol. 38, no. 9, pp. 1045–1062, 2019.
- [25] M. Ryll, D. Bicego, and A. Franchi, "Modeling and control of FAST-Hex: a fully-actuated by synchronized-tilting hexarotor," in *2016 IEEE/RSJ Int. Conf. on Intelligent Robots and Systems*, Daejeon, South Korea, Oct. 2016, pp. 1689–1694.
- [26] A. Franchi, R. Carli, D. Bicego, and M. Ryll, "Full-pose tracking control for aerial robotic systems with laterally-bounded input force," *IEEE Trans. on Robotics*, vol. 34, no. 2, pp. 534–541, 2018.
- [27] A. Franchi and A. Mallet, "Adaptive closed-loop speed control of BLDC motors with applications to multi-rotor aerial vehicles," in *2017 IEEE Int. Conf. on Robotics and Automation*, Singapore, May 2017, pp. 5203–5208.
- [28] G. Michieletto, M. Ryll, and A. Franchi, "Fundamental actuation properties of multi-rotors: Force-moment decoupling and fail-safe robustness," *IEEE Trans. on Robotics*, vol. 34, no. 3, pp. 702–715, 2018.
- [29] M. Faessler, A. Franchi, and D. Scaramuzza, "Differential flatness of quadrotor dynamics subject to rotor drag for accurate tracking of high-speed trajectories," *IEEE Robotics and Automation Letters*, vol. 3, no. 2, pp. 620–626, 2018.
- [30] F. Morbidi, D. Bicego, M. Ryll, and A. Franchi, "Energy-efficient trajectory generation for a hexarotor with dual-tilting propellers," in *2018 IEEE/RSJ Int. Conf. on Intelligent Robots and Systems*, Madrid, Spain, Oct. 2018.
- [31] T. Lee, M. Leoky, and N. H. McClamroch, "Geometric tracking control of a quadrotor UAV on SE(3)," in *49th IEEE Conf. on Decision and Control*, Atlanta, GA, Dec. 2010, pp. 5420–5425.
- [32] R. Mahony, S.-H. Cha, and T. Hamel, "A coupled estimation and control analysis for attitude stabilisation of mini aerial vehicles," in *2006 Australasian Conf. on Robotics & Automation*, Auckland, New Zealand, Nov. 2006, pp. 3003–3012.
- [33] R. M. Murray, Z. Li, S. S. Sastry, and S. S. Sastry, *A mathematical introduction to robotic manipulation*. CRC press, 1994.



Markus Ryll is Professor of Autonomous Aerial Systems in the Department of Aerospace and Geodesy at TU Munich. He obtained a Diploma in Mechatronics in 2008, a Master Degree in medical engineering in 2010 and received the Ph.D. degree from the Max Planck Institute for Biological Cybernetics in Tübingen, Germany in 2015. From 2014 to 2017 Markus was a Research Scientist at the RIS team at LAAS-CNRS, Toulouse, France. From 2018 to 2020 he served as Senior Research Scientist at the Robust Robotics Group at the Massachusetts Institute of Technology, Cambridge, USA.



Davide Bicego is a Post-Doctoral Researcher at the University of Twente, Enschede, The Netherlands, in the group of Robotics and Mechatronics (RAM). From 2016 to 2019, he carried out a Ph.D. at the Laboratoire d'Analyse et d'Architecture des Systèmes (LAAS-CNRS), Toulouse, France, in the Robotics and Interactions (RIS) group. He received the B.Sc. and the M.Sc. degrees in Information Engineering and Automation Engineering in 2013 and 2015, respectively, from University of Padua, Padua, Italy.



Mattia Giurato received the B.Sc. and the M.Sc. degrees in Automation and Control Engineering (in 2013 and 2015 respectively) from Politecnico di Milano and he concluded in 2020 his Ph.D. in Aerospace Engineering in the Aerospace Science and Technology department of Politecnico di Milano. He is now a Post-Doctoral Researcher in the Aerospace System and Control Laboratory (ASCL).



Marco Lovera (M98) is a Professor of Automatic Controls at the Politecnico di Milano. After a one-year period in industry he joined in 1999 the Dipartimento di Elettronica, Informazione e Bioingegneria of the Politecnico di Milano. Since 2015 he is with the Dipartimento di Scienze e Tecnologie Aerospaziali of the Politecnico di Milano, where he leads the Aerospace Systems and Control Laboratory (ASCL).



Antonio Franchi (S'07-M'11-SM'16) is a Professor of Robotics in the Faculty of Electrical Engineering, Mathematics & Computer Science, at the University of Twente, Enschede, The Netherlands, and an Associate Researcher at LAAS-CNRS, Toulouse, France. His main research interests include the design and control for robotic systems with applications to multi-robot systems and aerial robots. He co-authored more than 130 papers in peer-reviewed international journals and conferences.

Supplemental Material: FAST-Hex – A Morphing Hexarotor: Design, Mechanical Implementation, Control and Experimental Validation

Markus Ryll¹, Davide Bicego^{4,2}, Mattia Giurato³, Marco Lovera³ and Antonio Franchi^{4,2}

Abstract—This document presents additional experimental results for the article *FAST-Hex – A Morphing Hexarotor: Design, Mechanical Implementation, Control and Experimental Validation*. In this experiment the hexarotor is disturbed by a constant force while changing between under- to full actuation.

I. EXPERIMENTAL VALIDATION

A. Experiment 3: Force Disturbance

In this last experiment, we discuss the response of the FAST-Hex and of its controller with respect to external disturbances. To do this, we attached a rope close to the FAST-Hex’s CoM and apply to it a constant force $\mathbf{F}_D^W = [4.2 \ 0 \ 0]^T$ N thanks to a free hanging mass and a pulley. In this way, we emulated the scenarios of a constant wind disturbance or a contact-based inspection task. This experiment provides insights on how the controller and the FAST-Hex cope with disturbances during different configurations. Also in this case, we linearly increased the tilting angle α throughout the test.

The results of the experiment are depicted in Fig. ???. This time, the plots are visually separated into three phases. In the first one, the FAST-Hex is under-actuated (background of the plots is highlighted in red); in the second one (highlighted in yellow) the tilting angle α is greater zero, thus the robot gradually gains the MDT capability, but the feasible lateral forces are not large enough to fully compensate the lateral force disturbance; finally, in the last phase (highlighted in green) the disturbance force can be fully compensated.

The position tracking error is marginal ($\|\mathbf{e}_p\| = 5.8$ mm) during all conditions but gets significantly smaller from phase to phase (see plot 2). During the first one, the desired pitch angle needs to diverge from the reference pitch angle by approximately $\theta_d - \theta_r = -6.6^\circ$ to reorient the uni-directional force vector. Indeed, this is the only way to compensate the external disturbance (see plot 4). With an increasing tilting angle (see plot 8) the magnitude of the feasible and actual horizontal body force increases (see plot 5 and 7) allowing θ_d to converge towards θ_r (see plot 4). Once the tilting angle α is increased further beyond 25° , the platform is able to fully resist the force disturbance while tracking the reference orientation. This becomes more clear by inspecting plot 6 and 7 of Fig. ??, where we depict the rotor spinning velocities and both the feasible and actual lateral force module in body frame.

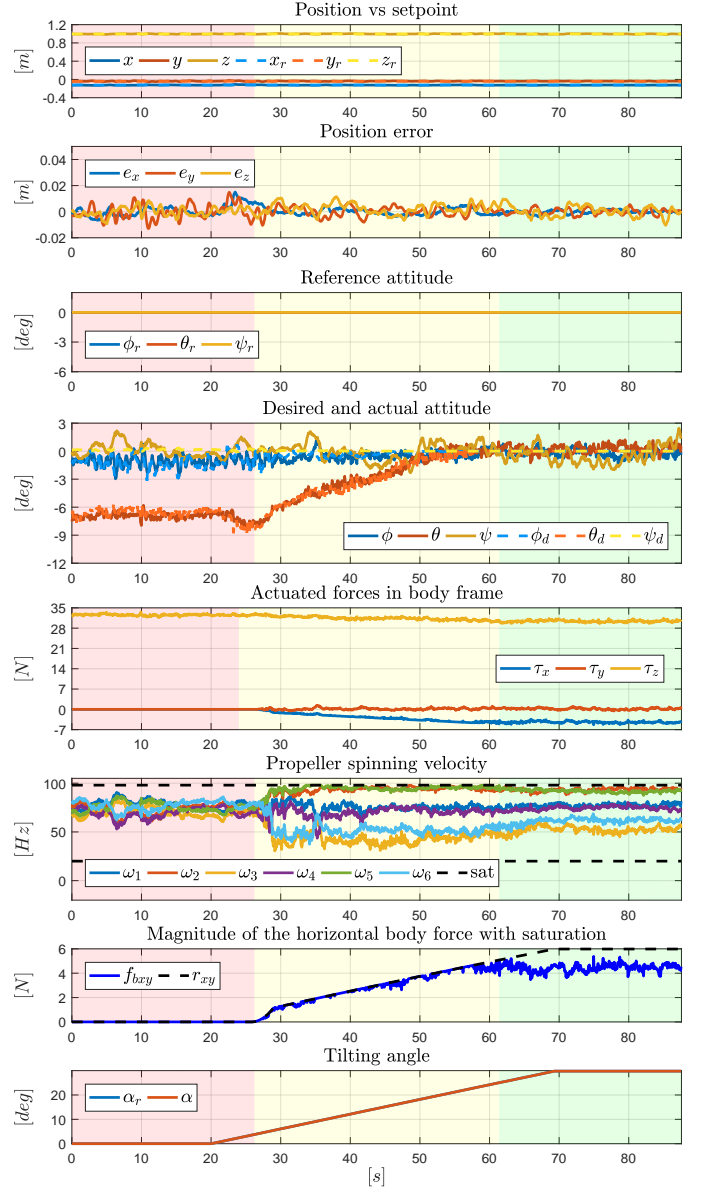


Fig. 1. Plots of Experiment 3 - from top to bottom. 1) Actual vs reference position; 2) Position tracking error; 3) Reference attitude depicted in Euler angles; 4) Desired and actual attitude depicted in Euler angles; 5) Actuated forces in body frame; 6) Actual propeller spinning velocity; 7) Maximum and actual lateral force; 8) Reference and actual tilting angle. While the FAST-Hex is under-actuated, the plots are highlighted in red, during full actuation, the plots are highlighted in green.

ACKNOWLEDGEMENTS

We thank Anthony Mallet (LAAS-CNRS) for his contribution in the software architecture of the experiments.

¹Computer Science and Artificial Intelligence Laboratory, Massachusetts Institute of Technology, Cambridge, USA, ryll@mit.edu

²LAAS-CNRS, Université de Toulouse, CNRS, Toulouse, France

³Dipartimento di Scienze e Tecnologie Aerospaziali, Politecnico di Milano, Milano, Italy, mattia.giurato@polimi.it

⁴Robotics and Mechatronics lab, Faculty of Electrical Engineering, Mathematics & Computer Science, University of Twente, Enschede, The Netherlands, {d.bicego, a.franchi}@utwente.nl

This work has been partially funded by the European Union’s Horizon 2020 research and innovation programme under grant agreement ID: 871479 AERIAL-CORE.